Title

Spatially Adaptive Varying Correlation Analysis for Multimodal Neuroimaging Data.

Journal

IEEE Transactions on Medical Imaging, 38(1)

Authors

Li, Lexin

Kang, Jian

Lockhart, Samuel

et al.

Publication Date

2019

DOI

10.1109/TMI.2018.2857221

Peer reviewed

Published in final edited form as:

IEEE Trans Med Imaging. 2019 January ; 38(1): 113–123. doi:10.1109/TMI.2018.2857221.

Spatially Adaptive Varying Correlation Analysis for Multimodal Neuroimaging Data

Lexin Li,
Division of Biostatistics, University of California at Berkeley, Berkeley, CA 94720, USA.

Jian Kang,
Department of Biostatistics, University of Michigan, Ann Arbor, MI 48109, USA.

Samuel N. Lockhart,
Department of Internal Medicine, Wake Forest School of Medicine, Winston-Salem, NC 27101, USA.

Jenna Adams, and
Helen Wills Neuroscience Institute, University of California, Berkeley, CA 94720, USA.

William J. Jagust
School of Public Health and Helen Wills Neuroscience Institute, University of California at Berkeley, and Lawrence Berkeley National Laboratory, Berkeley, CA 94720, USA.

Abstract

In this article, we study a central problem in multimodal neuroimaging analysis, i.e., identification of significantly correlated brain regions between multiple imaging modalities. We propose a spatially varying correlation model and the associated inference procedure, which improves substantially over the common alternative solutions of voxel-wise and region-wise analysis. Compared to voxel-wise analysis, our method aggregates voxels with similar correlations into regions, takes into account spatial continuity of correlations at nearby voxels, and enjoys a much higher detection power. Compared to region-wise analysis, our method does not rely on any pre-specified brain region map, but instead finds homogenous correlation regions adaptively given the data. We applied our method to a multimodal positron emission tomography study, and found brain regions with significant correlation between tau and glucose metabolism that voxel-wise or region-wise analysis failed to identify. Our findings conform and lend additional support to prior hypotheses about how the two pathological proteins of Alzheimer's disease, tau and amyloid, interact with glucose metabolism in the aging human brain.

Keywords

Alzheimer's disease; Graph partition; Multi-modal neuroimaging; Positron emission tomography; Varying coefficient model

Correspondence to: Lexin Li.

I. Introduction

Multimodal neuroimaging acquires different types of images for a common set of experimental subjects. It utilizes different physical and physiological sensitivities of imaging scanners and technologies, and measures distinct brain characteristics, ranging from brain structure and function to numerous chemical constituents. Multimodal analysis aggregates such diverse but often complementary information. Accumulated evidence has shown that multimodal analysis both improves our understanding of the brain and increases accuracy of neurological disorder diagnosis; see, e.g., [1]–[4], among others.

In multimodal neuroimaging analysis, one of the central problems is to understand the association between two or more imaging modalities, and to identify brain regions where such an association is statistically significant. For instance, joint analysis of functional magnetic resonance imaging (fMRI) and diffusion tensor imaging reveals the underlying interplay between brain function and structure [5], [6]. Analysis of fMRI and electroencephalography shows joint response of certain brain functions in certain brain regions [7]. Our motivation is a multimodal positron emission tomography (PET) study. The goal is to better understand the mechanism by which accumulation of different aggregated proteins, in this case, tau and beta-amyloid ($A\beta$), influences a third modality, glucose metabolism, in the aging human brain. Both tau and beta-amyloid are hallmark pathological proteins believed to be part of the driving mechanism of Alzheimer's disease. In our study, we seek to examine associations between tau accumulation, measured with the [^{18}F]AV-1451 tracer (AV-1451 PET), and reduced glucose metabolism, measured with the [^{18}F]Fluorodeoxyglucose tracer (FDG PET). Furthermore, this relationship may vary with a third chemical process of $A\beta$ accumulation, measured using the [^{11}C]Pittsburgh Compound B tracer (PiB PET). To investigate how early tau accumulation interacts with $A\beta$ to produce cortical hypometabolism, it is necessary to develop a method that can detect subtle but significant relations between multimodal PET data, i.e., AV-1451 PET and FDG PET, conditional on PiB PET and some other confounding covariates.

There are two common strategies to find significantly correlated brain regions between multiple imaging modalities. The first is voxel-wise analysis. That is, one calculates the correlation and conducts a significance test at every brain voxel location. Since there are typically 10^5 to 10^6 voxels in a brain image, multiple testing correction is employed after the voxel-wise tests. This type of analysis often suffers from particularly low detection power, due to the huge number of tests to correct and usually a very limited sample size. Besides, spatial correlation among brain voxels is often ignored. The second common solution is region-wise analysis. That is, one adopts a pre-specified brain atlas, averages the voxel values within each region-of-interest (ROI), then computes the region-wise correlation between multiple modalities. Multiple testing correction is also employed, but since the number of ROIs is typically 10^2, this approach enjoys a higher power than the voxel-wise solution. On the other hand, the voxels within the same ROI may not always share the same correlation pattern. Averaging voxels within ROIs may weaken or even cancel out significant correlations. In Section V–B, we review a number of related methods. Although they addressed the problems that are related to our between-modality correlation analysis, those methods either are not directly applicable to our problem, or suffer similar limitations as

those voxel-wise or region-wise solutions. There is a clear demand for an effective and powerful statistical procedure to identify significantly associated brain regions between multiple imaging modalities.

In this article, we propose a spatially varying correlation model and the associated inference procedure for multimodal analysis. Spatially varying coefficient models have been widely used in neuroimaging analysis [8]–[13], though often for a different purpose. We employ this model so to formally define the population parameter of interest in our investigation, i.e., the spatially varying correlation coefficient between multiple modalities. Based on this model, we then introduce a homogeneous spatial structure on the correlation coefficient. This structure is scientifically plausible, as spatially contiguous voxels often exhibit similar correlation patterns. We then develop a multi-step inferential procedure to estimate and infer about this correlation structure. Specifically, we first fit a spatially varying correlation model to each imaging modality, and obtain a sample correlation estimate at each voxel location. We then perform a kernel smoothing on the estimated voxel-wise correlations, which accounts for spatial continuity among adjacent voxels. After smoothing, we apply a graph clustering algorithm to partition the brain into regions with homogeneous correlations. Finally, we employ the maximum likelihood approach to estimate the region-level correlation given the estimated partitions. We carry out a likelihood ratio test for each partition, with a proper false discovery control, to test if the region-wise correlation is significantly different from zero or not. Figure 1 shows a schematic summary of our proposed inference procedure.

The key contribution of our proposal lies in the integration of voxel-wise and region-wise analysis. Compared to the traditional voxel-wise analysis, our approach accounts for spatial continuity of correlations at nearby voxels through spatial smoothing, and aggregates voxels with similar correlations into spatially homogeneous regions through our imposed correlation structure. The test is then carried out at the region level, instead of the voxel level, which substantially improves the detection power than a voxel-wise test. Compared to the traditional region-wise analysis, on the other hand, our method does not rely on any pre-specified brain region atlas, but instead finds homogenous correlation regions adaptively given the data. This adaptive approach avoids the potential issue that voxels in the same pre-defined region have opposite correlation patterns, and is to further improve the detection power.

We applied our method to a multimodal PET study, and found brain regions with significant correlation between tau and glucose metabolism that neither voxel-wise nor region-wise methods could find. The pattern of our findings conforms to prior hypotheses on how tau and glucose metabolism might be related, providing increased confidence in the method.

II. Material and Image Processing

A. Participants

Forty-seven cognitively normal older adults from the ongoing longitudinal Berkeley Aging Cohort Study [14] received structural MRI, [^{11}C]PiB, [^{18}F]FDG, and [^{18}F]AV-1451 PET

imaging. Eligibility requirements have been described previously [15]. Table I summarizes the participant demographics.

B. Image acquisition

All imaging was performed at Lawrence Berkeley National Laboratory (LBNL). [^{11}C]PiB was synthesized using a previously described protocol [16]. PiB PET imaging was performed in 3D acquisition mode using either an ECAT EXACT HR scanner ($n = 6$) or a BIOGRAPH PET/CT Truepoint 6 scanner ($n = 41$), both Siemens Medical Systems, Germany. PiB distribution volume ratio (DVR) values are not significantly different between scanners used. PiB imaging was attenuation corrected, and reconstructed using an ordered subset expectation maximization algorithm with weighted attenuation, scatter correction, and smoothed with a 4 mm Gaussian kernel. [^{18}F]FDG PET imaging was performed within an average of six days of PiB PET imaging using the same PET scanner, with images smoothed using a 4mm Gaussian kernel with scatter correction. [^{18}F]AV-1451 PET imaging was performed exclusively on the BIOGRAPH PET/CT scanner. AV-1451 was synthesized as described previously [17], and was reconstructed in a similar fashion as PiB imaging. All participants underwent a high-resolution T1-weighted magnetization prepared rapid gradient echo (MPRAGE) scan (TR/TE = 2110/3.58 ms, FA = 15°, 1 × 1 × 1 mm resolution) on a 1.5T Siemens Magnetom Avanto MRI scanner.

C. Image preprocessing

PiB images were realigned, and frames corresponding to the first 20 min of acquisition were averaged and coregistered to the participant's MRI. Voxel-wise DVR images were generated using Logan graphical analysis (35–90 min postinjection, cerebellar gray matter [GM] reference region)[18], and subject global PiB averages were calculated using native-space FreeSurfer cortical GM masks to characterize Aβ-positivity [15]; 21 subjects were classified as Aβ-positive. AV-1451 images were realigned, and the mean of all frames was used for coregistration to each participant's MRI. We created AV-1451 standardized uptake value (SUV) images based on mean tracer uptake over 80–100 min postinjection. We then normalized SUV images to a FreeSurfer defined cerebellar GM reference region [17] to create native-space voxel-wise SUV ratio (SUVR) images for each participant. FDG images were realigned, and the mean of all frames was used to coregister to MRI. We created FDG SUV images based on mean tracer uptake over 30–60 min postinjection. We then normalized SUV images to a pons reference region (manually edited from the FreeSurfer brainstem segmentation) to create native-space voxel-wise FDG SUVR images. We chose the reference region, such as cerebellum or pons, for normalization, since those regions are unlikely to be affected by the disease process and their use as reference for PET analysis has longstanding support [19]–[21]. T1 MPRAGE scans were processed using FreeSurfer v5.3 to delineate anatomical ROI masks for multiple brain regions on the native space MRI, coregistered to the PET scans [14]; we manually checked segmentations for accuracy. The reference region masks used for PiB, AV-1451, and FDG PET were derived this way. Importantly, the same subject MRI scan was used for all PET modalities in the current study.

D. Template space normalization and voxel based morphometry processing

We warped MRI scans for all subjects to the FSL MNI152 2mm space template using Advanced Normalization Tools as described previously [17]. Transformations were concatenated and applied to the coregistered AV-1451 and FDG PET images to generate MNI-space PET images. A testing mask was created using cortical brain regions on the AAL atlas [22] intersected with high-probability GM voxels (SPM12 tissue probability map with $p > 0.3$). MNI-space FDG and AV-1451 PET images were masked by this testing mask and smoothed by an additional 4mm FWHM gaussian kernel before analysis.

Voxel based morphometry (VBM) was performed using SPM12. T1 images were segmented, warped to an average template, normalized to MNI space using a 10mm FWHM smoothing kernel, and masked by the above testing mask. Smoothed modulated gray matter images were used as a measure of regional tissue volume at the voxel-wise level.

III. Method

To identify statistically significantly correlated brain locations between multiple imaging modalities, we introduce a varying correlation coefficient model. This model allows us to formally define the population parameter of interest, i.e., the spatially varying correlation coefficient between modalities. We next impose a homogeneous spatial structure on this correlation coefficient. Through this structure, we effectively integrate voxel-wise and region-wise analysis. We then develop a multi-step procedure to estimate and infer about this structure, and carry out the significance tests.

A. Spatially varying correlation model

Suppose the multimodal imaging data are collected from n subjects. Let $X_i(v)$, $Y_i(v)$, $Z_i(v)$ denote the measure of three imaging modalities at location v for subject i, $v = 1, \ldots, V$, and $i = 1, \ldots, n$. Let $\boldsymbol{C}_i = (C_{i,1}, \ldots, C_{i,p})^{\mathrm{T}}$ denote the vector of subject-level confounding covariates. Our goal is to infer the correlation between $X_i(v)$ and $Y_i(v)$, conditional on $Z_i(v)$ and $\boldsymbol{C}_i$, at locations $v = 1, \ldots, V$, and we seek those locations where this correlation is significantly different from zero. As an example, in our multimodal PET study, $X_i(v)$ and $Y_i(v)$ represent the tau PET and FDG PET imaging, $Z_i(v)$ represents the VBM imaging, and $\boldsymbol{C}_i$ collects subject's covariates such as age and sex. We consider the following varying correlation coefficient model,

$$X_i(v) = Z_i(v)\theta(v) + \boldsymbol{C}_i^{\mathrm{T}}\boldsymbol{\alpha}(v) + \epsilon_i(v), \quad (1)$$

$$Y_i(v) = Z_i(v)\eta(v) + \boldsymbol{C}_i^{\mathrm{T}}\boldsymbol{\beta}(v) + \varepsilon_i(v),$$

where $\theta(v)$, $\eta(v)$ are the spatially varying coefficients that account for the effect of the voxel-level confounder $Z_i(v)$, and $\boldsymbol{\alpha}(v)$, $\boldsymbol{\beta}(v)$ are the spatially varying coefficient vectors that

account for the effect of the subject-level confounding vector $\boldsymbol{C}_i$. The error terms $\epsilon_i(v)$ and $\varepsilon_i(v)$ satisfy that $E\{\epsilon_i(v)\} = E\{\varepsilon_i(v)\} = 0$, $\mathrm{Var}\{\epsilon_i(v)\} = \sigma_\epsilon^2(v)$, $\mathrm{Var}\{\varepsilon_i(v)\} = \sigma_\varepsilon^2(v)$. Furthermore,

$$\mathrm{Cov}\{\epsilon_i(v), \varepsilon_i(v)\} = \sigma_\epsilon(v)\sigma_\varepsilon(v)\rho(v), \quad (2)$$

where $\sigma_\epsilon(v) > 0$, $\sigma_\varepsilon(v) > 0$, and $-1 \le \rho(v) \le 1$. Similar varying coefficient models have been commonly examined and applied in neuroimaging analysis [8]–[13], though often for a completely different purpose; see Section V–B for more discussion. Model (1) leads to a formal definition of the primary object of interest for our multimodal analysis, i.e., the *same-location correlation coefficient*, $\rho(v)$, as defined in (2). We briefly comment that, the *cross-location correlation coefficient*, $\rho(v, v')$ from $\mathrm{Cov}\{\epsilon_i(v), \varepsilon_i(v')\} = \sigma_\epsilon(v)\sigma_\varepsilon(v')\rho(v, v')$, $1 \le v, v' \le V$, $v \ne v'$, is of scientific interest too, but is not the focus of this article.

Intuitively, the correlations between imaging modalities are similar in brain regions of spatially contiguous voxels. As such, it is reasonable to introduce a homogenous correlation structure within those regions. Particularly, we assume that there exist G non-overlap subgroups of all the brain voxels, denoted by $\{\mathscr{R}_g\}_{g=1}^G$ with $\mathscr{R}_g \cap \mathscr{R}_{g'} = \varnothing$ for $g \ne g'$, such that

$$\rho(v) = \sum_{g=1}^{G} r_g I[v \in \mathscr{R}_g], \quad (3)$$

where $-1 \le r_g \le 1$, with $\min_{1 \le g \le g' \le G} |r_g - r_{g'}| > 0$, and $I(\cdot)$ is an event indicator function with $I(\mathscr{A}) = 1$ if $\mathscr{A}$ occurs and $I(\mathscr{A}) = 0$ otherwise. This homogeneous correlation structure plays a central role in our proposed solution that integrates voxel-wise analysis with region-wise analysis. It tackles correlation at the individual voxel level, meanwhile shares the same spirit as region-wise analysis, in that it pools voxels with similar correlation patterns together. But unlike region-wise analysis, we do *not* assume the partition $\{\mathscr{R}_g\}_{g=1}^G$ is known *apriori*. Instead, we seek to adaptively estimate this partition, including the number of subgroups G, given the data. The resulting estimated homogenous regions do *not* have to coincide with those predefined brain atlas regions.

B. Model inference

We next develop an inferential procedure to estimate and infer the varying correlation coefficient $\rho(v)$ in (2) under model (1) and the homogeneous structure (3). We describe our procedure by steps. For each step, there are multiple choices, and we choose only one in our implementation. We discuss some alternative choices in Section V–C.

1) Sample correlation estimation: Given the data, we first fit model (1) using the least squares approach to obtain an estimate of the residuals, $\hat{\epsilon}_i(v)$ and $\hat{\varepsilon}_i(v)$. We then obtain the sample correlation estimate for $\rho(v)$, denoted as $\tilde{\rho}(v)$,

$$\tilde{\rho}(v) = \widehat{\mathrm{Corr}}\left(\left\{\hat{\varepsilon}_i(v)\right\}_{i=1}^{n}, \left\{\hat{\varepsilon}_i(v)\right\}_{i=1}^{n}\right).$$

Note that, for our analysis, the primary interest is the spatially varying correlation coefficient $\rho(v)$, instead of the varying coefficients $\theta(v)$, $\eta(v)$, $\boldsymbol{\alpha}(v)$, and $\boldsymbol{\beta}(v)$ that account for the effect of other confounding variables. As such, the step of sample correlation estimation amounts to voxel-wise least squares regressions. On the other hand, the varying coefficient model (1) is crucial for a proper definition of our population parameter of interest $\rho(v)$ and the subsequent inferences. Moreover, measurement error in Z_i is to potentially affect the coefficient estimates, $\theta(v)$, $\eta(v)$, $\boldsymbol{\alpha}(v)$, $\boldsymbol{\beta}(v)$, and can in effect increase the overall noise level. Our analysis focuses on the correlation of the residual terms, and thus should remain valid.

2) Spatial smoothing: We next spatially smooth the sample correlation coefficient. This smoothing step is to incorporate spatial continuity of the correlations of the adjacent voxels, which in turn is to facilitate clustering of the voxels with similar correlation patterns into the same groups. We also remark that there is no need to z-transform the correlation coefficient, as we are not imposing any Gaussian distributional assumption on $\rho(v)$. As such there is no need to transform its range from $(-1, 1)$ to the real line.

Specifically, we perform a kernel smoothing on the sample correlation estimate, $\{\tilde{\rho}(v)\}_{v=1}^{V}$, using the exponential squared kernel. We denote the smoothed version of the estimate for $\rho(v)$ as $\hat{\rho}(v)$, where

$$\hat{\rho}(v) = \frac{\sum_{v'=1}^{V} \exp\{-\tau d(v, v')\}\tilde{\rho}(v)}{\sum_{v'=1}^{V} \exp\{-\tau d(v, v')\}}.$$

Here $d(v, v')$ is the Euclidian distance between the two locations v and v'. We set the smoothing parameter, the full width at half-maximum (FWHM), at 9mm, following [23]. We have experimented with other FWHM values such as 6mm and 10mm, and obtained similar results.

We make a few remarks. First, in addition to the above spatial smoothing of the sample correlation estimate, we often smooth the raw image using a Gaussian kernel in imaging preprocessing. Our method is not sensitive to the raw image smoothing, in that the final results are similar with or without this preprocessing step. On the other hand, the step of raw image smoothing is to greatly facilitate the voxel-wise analysis. To be consistent, we always pre-smooth the raw images in all our numerical analyses. Second, in addition to the exponential squared kernel, our method can work with other kernels, e.g., a kernel that incorporates a correlation component.

3) Graph-based partitioning: We next seek a data adaptive estimation, based on $\hat{\rho}(v)$, of the spatially homogeneous regions $\left\{\mathscr{R}_g\right\}_{g=1}^{G}$ as defined in (3). While there are multiple clustering methods available, we choose a clustering-on-graph approach. This approach is

computationally efficient and maintains the spatial contiguity of the identified voxels that form the regions of correlation homogeneity.

Toward that end, we first create a correlation type indicator, $\hat{\delta}(v) \in \{-1, 0, 1\}$, which denotes the negative, null, and positive correlation type, respectively, by thresholding the smoothed estimate $\hat{\rho}(v)$ at each voxel v,

$$\hat{\delta}(v) = I\left[\hat{\rho}(v) > \lambda_{+}\right] - I[-\hat{\rho}(v) > \lambda_{-}],$$

where λ_+ and λ_- are taken as the 95% percentile of $\{\hat{\rho}(v)\}_{v=1}^{V}$ and $\{-\hat{\rho}(v)\}_{v=1}^{V}$. We comment that the performance of the method depends on the choice of the percentile value. We have chosen 95% percentile for two reasons. First, loosely speaking, the 95% percentile of the correlation estimate can be thought of as a critical value under the significant level 0.05. This is due to that, under the null hypothesis that the correlation is zero, the marginal distribution of the estimated correlation can be viewed as a rough approximation to the null distribution of the test statistic. Second, our simulations have suggested that the empirical performance under the 95% percentile achieves a good balance between sensitivity, specificity and FDR; see Table II in Section IV–A.

Next we construct two graphs, $\mathcal{G}_{+} = \left(\mathcal{E}_{+}, \mathcal{V}_{+}\right)$ and $\mathcal{G}_{-} = (\mathcal{E}_{-}, \mathcal{V}_{-})$, where

$$\mathcal{E}_{+} = \left\{(v, v') : d(v, v') < \tilde{d}, \delta(v) = \delta(v') = 1\right\},$$

$$\mathcal{V}_{+} = \left\{v : \delta(v) = 1\right\},$$

$$\mathcal{E}_{-} = \left\{(v, v') : d(v, v') < \tilde{d}, \delta(v) = \delta(v') = -1\right\}$$

$$\mathcal{V}_{-} = \{v : \delta(v) = -1\}.$$

Here the graph edges indicate whether the two voxels v and v' are close enough within the same graph, where $\tilde{d}$ is a distance measure threshold, and we set $\tilde{d} = 3$. We have also experimented with some other values of $\tilde{d}$, and the results are relatively stable, as long as $\tilde{d}$ is smaller than the value of FWHM; see Table III in Section IV–A. We then employ a graph clustering approach, the depth-first-search algorithm, to obtain the partition. This algorithm is particularly useful in saving the memory and speeding up the computation for graphs with a large number of nodes [24].

4) Likelihood ratio test with false discovery control: After obtaining the estimated group partition $\left\{\widehat{\mathcal{R}}_g\right\}_{g=1}^{\widehat{G}} = 1$, we propose to estimate the correlation coefficient r_g in (3)

using the maximum likelihood estimation approach. Subsequently, we test the significance of departure of r_g from zero using a likelihood ratio test, with a proper false discovery control. This likelihood based test is both computationally feasible and enjoys sound theoretical properties.

Specifically, the estimate $\hat{r}_g$ of r_g can be obtained by maximizing the log likelihood function for the data $\hat{\epsilon}_i(v)$ and $\hat{\eta}_i(v)$ within region $\hat{R}_g$. Denote $\boldsymbol{W}_{i,g} = \left[\left\{\hat{\epsilon}_i(v), v \in \widehat{\mathscr{R}}_g\right\}^{\mathrm{T}}, \left\{\hat{\eta}_i(v), v \in \widehat{\mathscr{R}}_g\right\}^{\mathrm{T}}\right]^{\mathrm{T}}$. This is equivalent to minimizing the following objective function,

$$n \log\det\left\{\boldsymbol{\Sigma}_g\left(r_g\right)\right\} + \sum_{i=1}^{n} \boldsymbol{W}_{i,g}^{\mathrm{T}} \boldsymbol{\Sigma}_g^{-1}\left(r_g\right) \boldsymbol{W}_{i,g},$$

with respect to r_g and other parameters in $\boldsymbol{\Sigma}_g(r_g)$, which is given by

$$\boldsymbol{\Sigma}_g\left(r_g\right) = \begin{pmatrix} \boldsymbol{\Sigma}_{x,g} & \boldsymbol{\Sigma}_{xy,g}\left(r_g\right) \\ \boldsymbol{\Sigma}_{xy,g}\left(r_g\right)^{\mathrm{T}} & \boldsymbol{\Sigma}_{y,g} \end{pmatrix},$$

where the diagonal elements of $\boldsymbol{\Sigma}_{xy,g}(r_g)$ equals r_g, and the off-diagonal elements unspecified. We recognize that the computation involved in this maximum likelihood estimation procedure can be expensive. To speed up the computation, we may impose $\boldsymbol{\Sigma}_{xy,g}\left(r_g\right) = r_g \mathbf{I}_{|\widehat{\mathscr{R}}_g|}$, where $|\widehat{\mathscr{R}}|$ denotes the number of voxels in region $\widehat{\mathscr{R}}$, and $\boldsymbol{I}_d$ is a d-dimensional identity matrix. This is equivalent to imposing that the cross-location correlation $\rho(v, v') = 0$. However, we remark that this assumption is only for computational simplicity. It is not crucial for our proposed procedure to work, and can be easily removed. We have compared the numerical results with and without this additional assumption, and found that the two results are similar.

Finally, we perform a likelihood ratio test on the series of hypotheses, $\hat{r}_g = 0$, $g = 1, \ldots, \widehat{G}$. Even though the test is carried out at the region level, it is still important to correct for multiple testing. In our implementation, we employ the method of [25] for false discovery rate (FDR) control. We report those regions whose corresponding correlations $\hat{r}_g$ are found significantly different from zero.

IV. Numerical Results

A. Simulation study

We first investigate the performance of our proposed method and its comparison to the alternative solutions through a simulation study. For ease of graphical illustration, we simulate the imaging data on 64 × 64 equally spaced grids in $[0, 1]^2$ according to the following model. For $i = 1, \ldots, n$,

$$X_i(v) = \xi_{i,1}(v) + \xi_{i,2}(v) + \epsilon_{i,0}(v),$$

$$Y_i(v) = \xi_{i,1}(v) - \xi_{i,2}(v) + \epsilon_{i,0}(v),$$

where $\xi_{i,k}$ follows a Gaussian process with mean zero and and covariance kernel κ_k, $k = 1, 2$. We set $\kappa_k(v,v') = \tau_k(v)\tau_k(v')\kappa_0(v,v')$ with $\kappa_0(v,v') = \exp\left(-10\|v - v'\|_2^2\right)$. We set $\tau_1^2(v) = 0.6\sum_{l=1}^{3} I\left(\|v - u_{1,l}\|_1 < 0.1\right)$, where $u_{1,1} = (0.3, 0.7)$, $u_{1,2} = (0.7, 0.7)$, and $u_{1,3} = (0.3, 0.3)$. We set $\tau_2^2(v) = 0.7\left\{I\left(\|v - u_{2,1}\|_1 < 0.1\right) + I\left(\|v - u_{2,2}\|_2 < 0.1\right)\right\}$, where $u_{2,1} = (0.5, 0.5)$ and $u_{2,2} = (0.7, 0.3)$ The random errors $\epsilon_{i,0}(v)$ and $\varepsilon_{i,0}(v)$ are mutually independent over i and v. Marginally, $\epsilon_{i,0}(v) \sim N\left\{0, s_1^2(v)\right\}$, and $\varepsilon_{i,0}(v) \sim N\left\{0, s_2^2(v)\right\}$ where $\log s_k^2(v)$ follows a Gaussian process with mean zero and covariance kernel $m_k\kappa_0$, $k = 1,2$. We consider three levels of signal strength, by setting $(m_1, m_2) = (0.15, 0.25)$ for a weak signal, $(m_1, m_2) = (0.45, 0.55)$ for a medium signal, and $(m_1, m_2) = (0.75, 0.85)$ for a strong signal. Under this setup,

$$\rho(v) = \frac{\tau_1^2(v) - \tau_2^2(v)}{\sqrt{\left\{\tau_1(v) + \tau_2(v)\right\} + s_1^2(v)}\sqrt{\left\{\tau_1(v) + \tau_2(v)\right\} + s_2^2(v)}}.$$

Figure 2, the top panel, shows the simulated imaging data for two random subjects, $\{X_1(v), Y_1(v)\}$, $\{X_2(v), Y_2(v)\}$ under a weak signal. We set the sample size $n = 50$, and the significance level $\alpha = 0.05$. We have also considered Cauchy errors, and the results (not reported here) are similar with a reasonable amount of outliers and signal strength.

We compare our proposed spatially adaptive method with two alternatives: the voxel-wise analysis and the region-wise analysis. Specifically, for the voxel-wise analysis, we perform the Pearson correlation test for each voxel and adjust the p-value with FDR control [25]. For the region-wise analysis, we consider 4 × 4 equally spaced region partitions. See Figure 2, bottom panel, top left quadrant, for the partitioned regions. We take the average of the imaging data within each region to obtain region specific imaging statistics. We then perform the region-wise correlation test, with the same multiple testing correction as the voxel-wise analysis. We remark that, a refined partition of regions such as 8 × 8 or 16 × 16 partitions would improve the sensitivity and specificity in this simulation example, though still underperforms than our proposed method. The larger the number of the partitioned regions, the closer it is to the voxel-wise analysis. So the size of the partition essentially reflects a tradeoff between region-wise and voxel-wise analysis. Moreover, we only use the grid-type partition for illustration purpose in our simulation. In practice, one rarely uses the grid partition, but often employs some prespecified brain atlas to partition the brain and to define the regions, within which the between-modality correlation may not always be homogeneous. Figure 2, the bottom panel, reports the selection results by the three methods based on one data replication.

Table II summarizes the mean and standard deviation (in parentheses) over 100 replications for sensitivity, specificity and FDR under three different signal strengths. We also examine the effect of pre-smoothing and the percentile thresholding value for λ_+ and λ_-. We make the following observations. First, our spatially adaptive method is seen to achieve the best performance. The voxel-wise method suffers from extremely low sensitivity, while the region-wise method suffers from high false discovery rate. Our proposed spatially adaptive method enjoys both competitive sensitivity and specificity, along with sound false discovery control. Second, the pre-smoothing step does not affect our method much, but is to facilitate the voxel-wise analysis. Third, the performance of our method does depend on the percentile thresholding value. We have experimented with two thresholding values, 90% and 95%. With the 90% threshold, our method enjoys a better sensitivity and specificity, but also suffers from a larger false discovery. With the 95% threshold, our method achieves a reasonable balance between sensitivity, specificity and FDR. In summary, our proposed method consistently outperforms the voxel-wise and region-wise solutions.

Finally, we examine the effect of $\tilde{d}$ in the graph construction step. Table III reports the results for the weak signal case with $\tilde{d}$ taking the value in {1, 2, 3, 4, 5, 7, 9, 10, 11}. We observe that, as long as $\tilde{d}$ is smaller than the FWHM value, the results are relatively stable, while the results can be affected if $\tilde{d}$ exceeds the FWHM value.

B. Multimodal PET analysis

We applied the proposed approach to the multimodal PET study introduced in Section II. Our goal was to examine associations between hypothesized increased tau accumulation and reduced glucose metabolism as a function of PiB status group, after controlling for local GM and other covariates. We fitted the model (1) to all the data, with the tau PET and FDG PET imaging serving as $X_i(v)$ and $Y_i(v)$, the VBM imaging as $Z_i(v)$, and subject's age and sex forming $\boldsymbol{C}_i$. We then carried out the correlation analysis based on the residuals for the Aβ-positive and Aβ-negative groups separately. We set the significance level at $\alpha = 0.05$, and declared a cluster significant if its *corrected p*-value after the FDR control is smaller than α. Besides, we removed those small clusters if the number of voxels is no more than 20.

We summarize the results in Figure 3 and Table IV. Among Aβ-negative participants (the left panel of Figure 3), increased AV-1451 uptake was significantly associated with reduced FDG metabolism in clusters located in bilateral medial temporal lobes (MTL). These clusters were localized to amygdala, hippocampus, and entorhinal cortex (anterior parahippocampal gyrus); Table IV reports AAL labels of cluster peaks and the cluster center coordinates. Additional smaller clusters were observed in inferior frontal cortex and temporo-occipital fusiform gyrus. Among Aβ-positive participants (the right panel of Figure 3), significant inverse AV-1451 and FDG associations were located in right inferolateral temporal, and bilateral medial parietal and inferior medial frontal cortex. Importantly, correlations of increased AV-1451 with reduced FDG follow a pattern of tau accumulation reported by the pathology literature [19], with correlations observed in Aβ-negative subjects in regions known to first accumulate tau pathology such as MTL, and correlations observed in Aβ-positive subjects in later stage (temporal and parietal) regions. We also clarify that, the AAL atlas was not used in our detection method, but instead was only employed in Table IV

to facilitate the interpretation of our identified clusters of voxels. We further expand on our scientific findings in the discussion section.

We also note that, while our multimodal analysis focused on investigating associations between increased tau accumulation and reduced glucose metabolism, we did examine positive associations between FDG and AV-1451 as well. We observed some positively correlated clusters both before and after covarying for voxel-wise VBM data. Positive clusters occurred predominantly in the same areas in both subject groups; see Figure 4. They were primarily localized to the longitudinal fissure and lateral sulcus, in brain regions comprising tissue/CSF borders, and were decreased in volume after correction by VBM data (decreased by 24mm^3 in Aβ-negative, and 128mm^3 in Aβ-positive subjects), suggesting these clusters of correlations were related to partial volume (atrophy) effects in the data.

As a comparison, we also applied the alternative methods, the voxel-wise correlation analysis, and the region-wise correlation analysis using the AAL atlas. When analyzing the Aβ-negative group and the Aβ-positive groups separately, neither method found any significantly correlated regions after FDR correction, reflecting their low detection power. When analyzing the Aβ-negative and Aβ-positive groups jointly, neither method found any significantly negatively correlated regions. The two methods identified a number of significantly positively correlated regions, which we found are most likely attributed to the aforementioned atrophy effects.

V. Discussion and Conclusion

A. Scientific findings

In the current study, we sought to examine associations between tau and glucose metabolism, after controlling for local grey matter volume, and whether relationships varied with global Aβ burden. We found that in cognitively normal Aβ-negative older adults, tau deposition was associated primarily with reduced metabolism in MTL and in inferior frontal regions. In Aβ-positive elderly, increased tau deposition was associated with metabolic decline in medial frontal and parietal cortex, as well as in inferolateral temporal cortex. These results suggest that patterns of inverse associations between tau accumulation and glucose metabolism differ based upon amyloid status and are congruent with previous knowledge of the distribution of tau, Aβ, and hypometabolism in AD.

Importantly, correlations of increased AV-1451 with reduced FDG follow a pattern of tau accumulation that complies with the pathology literature [19], such that in normal older adults without substantial amyloid burden, correlations are found in regions known to first accumulate tau pathology such as MTL (Braak stages 1 and 2). In parallel to the neuropathological data, recent tau-PET data have demonstrated that age is associated with more tau accumulation in the MTL regardless of Aβ status [17]. Reduced glucose metabolism in the hippocampus has been widely reported in normal older individuals [26], normal older individuals who subsequently show cognitive decline [27], and patients with AD and mild cognitive impairment [28]. While there is evidence linking atrophy of the hippocampus to postmortem neurofibrillary tau pathology in aging and AD [29], studies of the pathological basis of hippocampal hypometabolism are lacking. The correspondence of

age-related tau pathology and age-related hippocampal hypometabolism, however, is consistent with our results that implicate tau as at least part of the underlying mechanism. In addition, the finding of tau-related hypometabolism in the medial parietal, inferior temporal, and medial prefrontal cortex that is related to the presence of Aβ is consistent with both extensive prior and recent data. Hypometabolism in the posterior cingulate has long been recognized as an early metabolic finding in AD [30] as has temporal lobe hypometabolism [31]. While inferomedial pre-frontal cortex has not been specifically identified as a typical region of AD hypometabolism, it is a brain region notably affected by both Aβ and tau deposition [17], [32]. Finally, a recent report points to the AD-like pattern of hypometabolism as associated with synergistic effects of Aβ and tau, while effects of tau alone are limited to the MTL [33].

B. Related methods

Our proposal is related to but also clearly distinct from a number of existing methods in the literature. The first related line of research is statistical parametric mapping, and in particular, the random field theory based method [34], and the multimodal analysis toolbox [35]. However, the focus of [34] is to correct the p-values of individual voxels from multiple testing through random field theory. The test is still carried out at the voxel-level, and is expected to suffer from low detection power of a typical voxel-wise analysis. On the other hand, the correction method of [34] can be employed in our multi-step inferential procedure, by replacing the FDR correction method of [25] in step 4. More recently, [35] developed a biological parametric mapping toolbox for multimodal analysis. While it offers improvements such as non-parametric and robust regression, it still suffers from the same limitations as voxel-wise or region-wise methods. Unlike our proposal, none of those methods provides a solution that combines voxel-wise and region-wise analysis. The second line of research includes numerous varying coefficient models, and relatedly, functional mixed effects models, for neuroimaging analysis [8]–[13]. The main distinction between our proposal and those existing varying coefficient based solutions is the primary parameter of interest. Our focus is the varying correlation coefficient $\rho(v)$ in (2) between multiple modalities under model (1), and we estimate and infer about $\rho(v)$ under the homogeneous spatial structure (3). By contrast, the primary target of the existing solutions are the varying coefficient effects, i.e., $\theta(v)$, $\eta(v)$, $\boldsymbol{\alpha}(v)$, and $\boldsymbol{\beta}(v)$ under model (1), and mostly for a single imaging modality. The third line concerns data-driven brain parcellation and homogeneous brain region identification, mostly in the context of brain connectivity analysis using fMRI data. See [36] for a review and the references therein. Again, this category of methods targets a different problem than ours. However, some of those data-driven parcellation methods can be employed in conjunction with our proposed inferential procedure, by replacing the graph-based partition method in step 3.

C. Future extensions

A key assumption of our solution is the correlation homogeneity assumption (3). This structure can greatly reduce the complexity of the subsequent statistical testing procedure, while losing relatively little information for detecting the true signals. This assumption can also be relaxed for extra modeling flexibility. For example, we may allow the correlations within a region to differ to some extent, and require that the correlation at each voxel to

depend on the correlations of its neighbors. This additional flexibility may further increase the detection power, and can reduce the false positive rate if the model is correctly specified. However, it also comes with a price, as it would inevitably introduce additional unknown parameters, and may lose efficiency when the sample size is limited. A balance between model flexibility and model complexity in this context is warranted for future investigation.

Our proposed inference is a multi-step procedure. For each step, one may consider some alternative solutions than the ones we currently employ. In step 1, we use the Pearson correlation. A potential alternative is to use a rank based correlation coefficient that may capture the nonlinear dependence between the two imaging modalities. In step 2, in addition to the exponential squared kernel and the Euclidian distance, other kernel functions or distance measures could be used [37]. Moreover, one may also consider other smoothing techniques, e.g., smoothing splines, than kernel smoothing. In step 3, we currently threshold the estimated correlation surface over the brain and find the connected voxels using a breath-first algorithm based on the graph theory. Alternative approaches, such as model-based clustering and spatially weighted *k*-means clustering, can serve as potential substitutes, though some of those methods may be computationally more intensive. In step 4, we employ the likelihood ratio test for assessing the statistical significance. Other testing procedures such as the Wald test and the score test can be used for the same purpose. Moreover, in addition to the asymptotical tests, the permutation test is another viable alternative. It generally requires fewer assumptions and thus is more flexible, though it could be highly intensive computationally. The final significant regions are identified after controlling the false discovery rate using the standard multiple comparison approach of [25]. Other FDR correction methods can be used as well; for instance, the FDR control based on the random field theory[34].

D. Conclusion

In this article, we focus on the analysis of spatially varying correlation patterns between two imaging modalities over the brain. One simple solution to this problem is to perform massively voxel-wise testing followed by multiple comparison corrections, which, as we have shown, suffers from extremely low statistical power to identify significant voxels when the sample size is relatively small. Alternatively, one can reduce the gigantic number of tests by turning to region-level inference using an existing brain atlas. This solution takes summary statistics for each region and then perform region-wise statistical tests. Its performance, however, heavily relies on the choice of the region partitions. For instance, a coarse region partition may produce larger regions that include both positively and negatively correlated regions, in which case, the region-wise test may fail to detect any type of correlation patterns. On the other hand, a finer region partition may use testing regions that are smaller than the true correlated regions, which would in turn reduce the power of the region-wise method to recover the true signals. The key of our proposal is to first evaluate the between-modality correlation at the voxel level, then adaptively aggregates those voxels which are spatially contiguous and share similar correlation patterns, then carry out the significance test at the region level. In effect, our method integrates voxel-wise and region-wise analysis, and thus overcomes those limitations and enjoys a much higher statistical power to detect the signals.

Although the mechanisms by which late-life tau and amyloid accumulation influence glucose metabolism are not well understood, our results suggest early tau accumulation interacts with Aβ to produce cortical hypometabolism, even among normal elderly. Furthermore, the method we have developed enhances neuroimaging research of aging and dementia by providing improved detection of results without need for massively voxel-wise testing or region-based partitioning. Both the biological and methodological components of this work represent useful advances to the field.

Acknowledgement

Li's work was partially supported by NSF grants DMS-1310319, DMS-1613137, and NIH grant AG034570. Kang's work was partially supported by NIH grant MH105561. Jagust's work was partially supported by NIH grant AG034570.

References

[1]. Hinrichs C, Singh V, Xu G, and Johnson SC, "Predictive markers for AD in a multi-modality framework: An analysis of MCI progression in the ADNI population," NeuroImage, vol. 55, no. 2, pp. 574–589, 2011. [PubMed: 21146621]

[2]. Zhang D, Wang Y, Zhou L, Yuan H, Shen D, and the Alzheimers Disease Neuroimaging Initiative, "Multimodal classification of Alzheimer's disease and mild cognitive impairment," Neuroimage, vol. 55, no. 3, pp. 856–867, 2011. [PubMed: 21236349]

[3]. Dai Z, Yan C, Wang Z, Wang J, Xia M, Li K, and He Y, "Discriminative analysis of early alzheimer's disease using multi-modal imaging and multi-level characterization with multi-classifier." NeuroImage, vol. 59, no. 3, pp. 2187–2195, 2012. [PubMed: 22008370]

[4]. Uludag K and Roebroeck A, "General overview on the merits of multimodal neuroimaging data fusion," NeuroImage, vol. 102, no. 1, pp. 3–10, 2014. [PubMed: 24845622]

[5]. Andrews-Hanna JR, Snyder AZ, Vincent JL, Lustig C, Head D,Raichle ME, and Buckner RL, "Disruption of large-scale brain systems in advanced aging," Neuron, vol. 56, no. 5, pp. 924–935, 2007. [PubMed: 18054866]

[6]. Zhu D, Zhang T, Jiang X, Hu X, Chen H, Yang N, Lv J, Han J,Guo L, and Liu T, "Fusing dti and fmri data: a survey of methods and applications," NeuroImage, vol. 102, pp. 184–191, 2014. [PubMed: 24103849]

[7]. Singh M, Kim S, and Kim T-S, "Correlation between bold-fmri and eeg signal changes in response to visual stimulus frequency in humans," Magnetic Resonance in Medicine, vol. 49, no. 1, pp. 108–114, 2003. [PubMed: 12509825]

[8]. Zhu H, Fan J, and Kong L, "Spatially varying coefficient model for neuroimaging data with jump discontinuities," Journal of the American Statistical Association, vol. 109, no. 507, pp. 1084–1098, 7 2014. [PubMed: 25435598]

[9]. Ge T, Mller-Lenke N, Bendfeldt K, Nichols TE, and Johnson TD, "Analysis of multiple sclerosis lesions via spatially varying coefficients," Ann. Appl. Stat, vol. 8, no. 2, pp. 1095–1118, 06 2014 [Online]. Available: 10.1214/14-AOAS718 [PubMed: 25431633]

[10]. Zhang F, Jiang W, Wong P, and Wang J-P, "A bayesian probit model with spatially varying coefficients for brain decoding using fmri data," Statistics in Medicine, vol. 35, no. 24, pp. 4380–4397, 2016, sim.6999. [Online]. Available: 10.1002/sim.6999 [PubMed: 27222305]

[11]. Hyun JW, Li Y, Gilmore JH, Lu Z, Styner M, and Zhu H, "Sgpp: spatial gaussian predictive process models for neuroimaging data," NeuroImage, vol. 89, pp. 70–80, 2014. [PubMed: 24269800]

[12]. Lin J-A, Zhu H, Mihye A, Sun W, and Ibrahim JG, "Functional mixed effects models for candidate genetic mapping in imaging genetic studies," Genetic epidemiology, vol. 38, no. 8, pp. 680–691, 12 2014 [Online]. Available: http://www.ncbi.nlm.nih.gov/pmc/articles/PMC4236266/ [PubMed: 25270690]

[13]. Yuan Y, Gilmore JH, Geng X, Martin S, Chen K, ling Wang J, and Zhu H, “Fmem: Functional mixed effects modeling for the analysis of longitudinal white matter tract data,” NeuroImage, vol. 84, no. Supplement C, pp. 753–764, 2014 [Online]. Available: http://www.sciencedirect.com/science/article/pii/S1053811913009567 [PubMed: 24076225]

[14]. Mormino EC, Kluth JT, Madison CM, Rabinovici GD, Baker SL, Miller BL, Koeppe RA, Mathis CA, Weiner MW, Jagust WJ, and the Alzheimer’s Disease Neuroimaging Initiative, “Episodic memory loss is related to hippocampal-mediated -amyloid deposition in elderly subjects,” Brain, vol. 132, no. 5, pp. 1310–1323, 05 2009. [PubMed: 19042931]

[15]. Mormino EC, Smiljic A, Hayenga AO, Onami SH, Greicius MD,Rabinovici GD, Janabi M, Baker SL, Yen IV, Madison CM,Miller BL, and Jagust WJ, “Relationships between beta-amyloid and functional connectivity in different components of the default mode network in aging,” Cerebral Cortex, vol. 21, no. 10, pp. 2399–2407, 10 2011. [PubMed: 21383234]

[16]. Mathis CA, Wang Y, Holt DP, Huang G-F, Debnath ML, and Klunk WE, “Synthesis and evaluation of 11c-labeled 6-substituted 2-arylbenzothiazoles as amyloid imaging agents,” Journal of Medicinal Chemistry, vol. 46, no. 13, pp. 2740–2754, 2003. [PubMed: 12801237]

[17]. Schöll M, Lockhart S, Schonhaut D, ONeil J, Janabi M, Ossenkoppele R, Baker S, Vogel J, Faria J, Schwimmer H, Rabinovici G, andJagust W, “PET imaging of tau deposition in the aging human brain,” Neuron, vol. 89, no. 5, pp. 971–982, 2016. [PubMed: 26938442]

[18]. Logan J, Fowler JS, Volkow ND, Wang G-J, Ding Y-S, andAlexoff DL, “Distribution volume ratios without blood sampling from graphical analysis of pet data,” Journal of Cerebral Blood Flow & Metabolism, vol. 16, no. 5, pp. 834–840, 1996. [PubMed: 8784228]

[19]. Braak H and Braak E, “Neuropathological stageing of alzheimer-related changes,” Acta Neuropathologica, vol. 82, no. 4, pp. 239–259, 1991. [PubMed: 1759558]

[20]. Thal DR, Rüb U, Orantes M, and Braak H, “Phases of a-deposition in the human brain and its relevance for the development of ad,” Neurology, vol. 58, no. 12, pp. 1791–1800, 2002 [Online]. Available: http://n.neurology.org/content/58/12/1791 [PubMed: 12084879]

[21]. Minoshima S, Frey KA, Foster NL, and Kuhl DE, “Preserved pontine glucose metabolism in alzheimer disease: a reference region for functional brain image (pet) analysis.” Journal of computer assisted tomography, vol. 19(4), pp. 541–547, 1995. [PubMed: 7622680]

[22]. Tzourio-Mazoyer N, Landeau B, Papathanassiou D, Crivello F,Etard O, Delcroix N, Mazoyer B, and Joliot M, “Automated anatomical labeling of activations in SPM using a macroscopic anatomical parcellation of the MNI MRI single-subject brain,” NeuroImage, vol. 15, no. 1, pp. 273–289, 2002. [PubMed: 11771995]

[23]. Worsley KJ, Marrett S, Neelin P, and Evans AC, “Searching scale space for activation in pet images,” Human Brain Mapping, vol. 4, no. 1, pp. 74–90, 1996 [Online]. Available: 10.1002/(SICI)1097-0193(1996)4:1⟨74::AID-HBM5⟩3.0.CO;2-M [PubMed: 20408187]

[24]. Even S, Graph Algorithms, 2nd ed New York, NY, USA: Cambridge University Press, 2011.

[25]. Benjamini Y and Yekutieli D, “The control of the false discovery rate in multiple testing under dependency,” Annals of Statistics, pp. 1165–1188, 2001.

[26]. Knopman DS, J. CR, Jr., Wiste HJ, Lundt ES, Weigand SD,Vemuri P, Lowe VJ, Kantarci K, Gunter JL, Senjem ML,Mielke MM, Roberts RO, Boeve BF, and Petersen RC, “18F-fluorodeoxyglucose positron emission tomography, aging, and apolipoprotein e genotype in cognitively normal persons,” Neurobiology of Aging, vol. 35, no. 9, pp. 2096–2106, 2014. [PubMed: 24702820]

[27]. de Leon MJ, Convit A, Wolf OT, Tarshish CY, DeSanti S,Rusinek H, Tsui W, Kandil E, Scherer AJ, Roche A, Imossi A,Thorn E, Bobinski M, Caraos C, Lesbre P, Schlyer D, Poirier J,Reisberg B, and Fowler J, “Prediction of cognitive decline in normal elderly subjects with 2-[18f]fluoro-2-deoxy-d-glucose/positron-emission tomography (fdg/pet),” Proceedings of the National Academy of Sciences, vol. 98, no. 19, pp. 10 966–10 971, 2001.

[28]. Chételat G, Desgranges B, Landeau B, Mézenge F, Poline JB,de la Sayette V, Viader F, Eustache F, and Baron J-C, “Direct voxel-based comparison between grey matter hypometabolism and atrophy in Alzheimer’s disease,” Brain, vol. 131, no. 1, p. 60, 2008. [PubMed: 18063588]

[29]. Jack C, Dickson D, Parisi J, Xu YC, Cha RH, O’Brien P,Edland SD, Smith GE, Boeve BF, Tangalos E, Kokmen E, and Petersen R, “Antemortem MRI findings correlate with hippocampal

neuropathology in typical aging and dementia," Neurology, vol. 58, no. 5, pp. 750–757, 03 2002. [PubMed: 11889239]

[30]. Minoshima S, Giordani B, Berent S, Frey KA, Foster NL, andKuhl DE, "Metabolic reduction in the posterior cingulate cortex in very early alzheimer's disease," Annals of Neurology, vol. 42, no. 1, pp. 85–94, 1997. [PubMed: 9225689]

[31]. Landau SM, Harvey D, Madison CM, Koeppe RA, Reiman EM,Foster NL, Weiner MW, and Jagust WJ, "Associations between cognitive, functional, and fdg-pet measures of decline in AD and MCI," Neurobiology of Aging, vol. 32, no. 7, pp. 1207–1218, 2011. [PubMed: 19660834]

[32]. Lockhart SN, Schöll M, Baker SL, Ayakta N, Swinnerton KN,Bell RK, Mellinger TJ, Shah VD, O'Neil JP, Janabi M, and Jagust WJ, "Amyloid and tau PET demonstrate region-specific associations in normal older people," NeuroImage, vol. 150, pp. 191–199, 2017. [PubMed: 28232190]

[33]. Hanseeuw BJ, Betensky RA, Schultz AP, Papp KV, Mormino EC, Sepulcre J, Bark JS, Cosio DM, LaPoint M, Chhatwal JP, Rentz DM, Sperling RA, and Johnson K, "Fdg metabolism associated with tau-amyloid interaction predicts memory decline," Annals of Neurology, p. in press, 2017.

[34]. Worsley KJ, Taylor JE, Tomaiuolo F, and Lerch J, "Unified univariate and multivariate random field theory," NeuroImage, vol. 23, pp. S189–S195, 2004. [PubMed: 15501088]

[35]. Casanova R, Srikanth R, Baer A, Laurienti PJ, Burdette JH,Hayasaka S, Flowers L, Wood F, and Maldjian JA, "Biological parametric mapping: A statistical toolbox for multimodality brain image analysis," NeuroImage, vol. 34, no. 1, pp. 137–143, 2007. [PubMed: 17070709]

[36]. Eickhoff SB, Thirion B, Varoquaux G, and Bzdok D, "Connectivity-based parcellation: Critique and implications," Human Brain Mapping, vol. 36, no. 12, pp. 4771–4792, 2015 [Online]. Available: 10.1002/hbm.22933 [PubMed: 26409749]

[37]. Hastie T, Tibshirani R, and Friedman J, The Elements of Statistical Learning, ser. Springer Series in Statistics. New York, NY, USA: Springer, 2001.

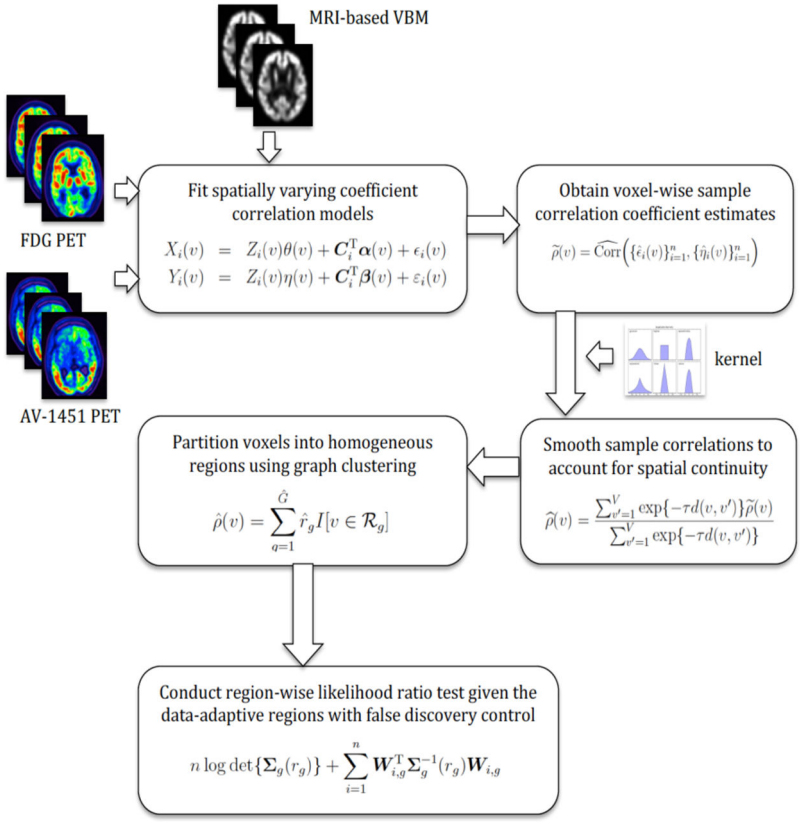

Fig. 1.
The schematic plot of the proposed inference procedure.

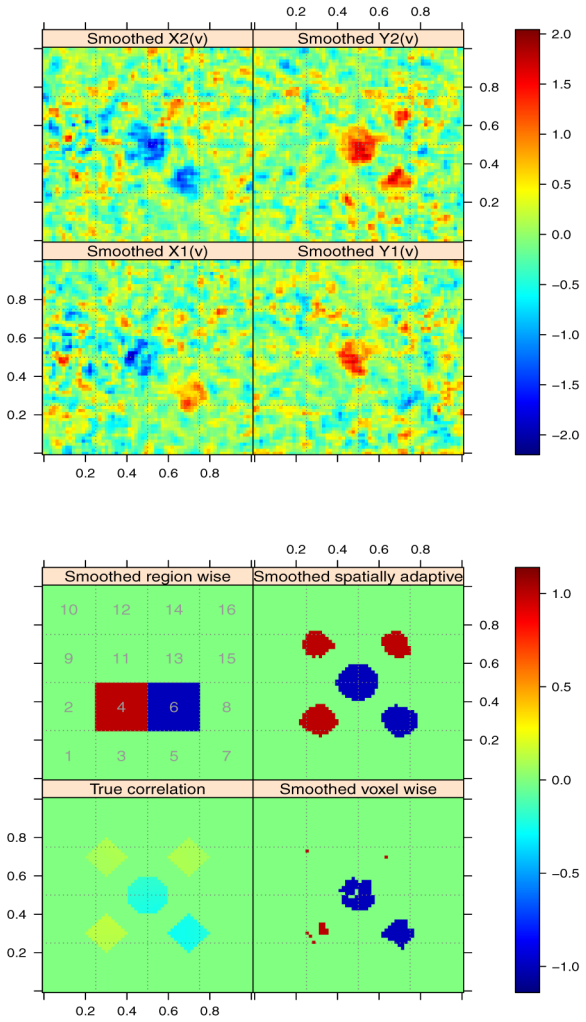

Fig. 2.

Illustration of the simulation study. Top panel: the simulated bivariate images for two random subjects. Bottom panel: the true correlation map (bottom left), and the significantly positively (red) and negatively (blue) correlated regions selected by the three methods: voxel-wise analysis (bottom right), region-wise analysis (top left), and our proposed spatially adaptive analysis (top right). The images were pre-smoothed before the analysis.

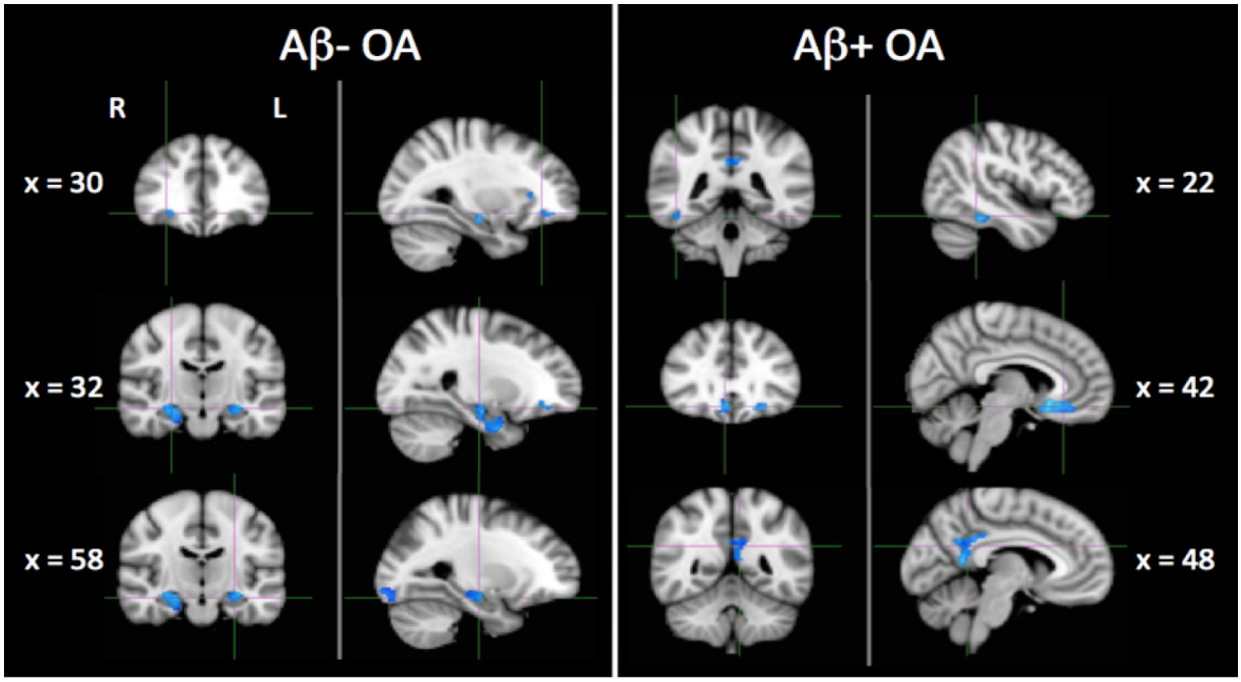

Fig. 3.

AV-1451 – FDG associations by Aβ status. Clusters indicate significant negative associations between AV-1451 and FDG in Aβ− (left) and Aβ positive (right) older adults (OA).

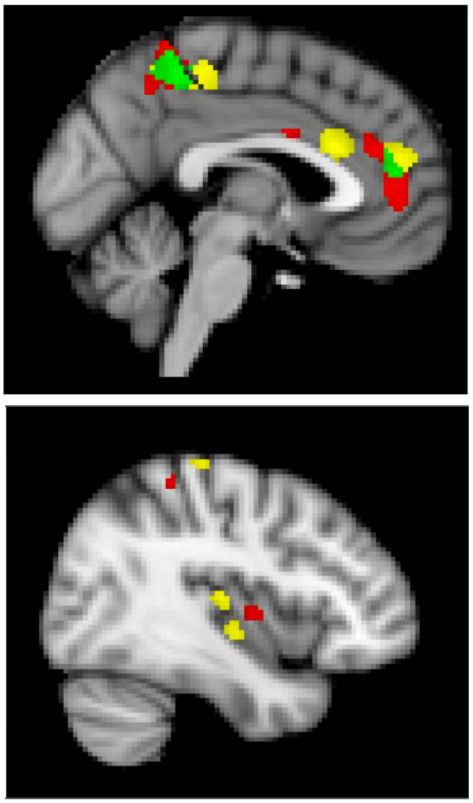

Fig. 4.

Positive correlations in FDG – AV1451 data. Positive clusters are visualized on the MNI template brain for Aβ-negative (red) and Aβ-positive (yellow) subjects (overlap: green). Positive clusters occurred predominantly in the same areas in both subject groups, primarily localized to the longitudinal fissure and lateral sulcus.

Table I

Demographic characteristics of the participants. Reported for each group is mean (standard deviation), or the number of participants (percentage), and the associated two-sample test statistic with the *p*-value. the last row reports the acquisition time difference between AV-1451 and FDG PET scans. A$\beta-$, Aβ-negative older adults; A$\beta+$, Aβ-positive older adults; ApoE4, Apolipoprotein E4; MMSE, Mini-Mental State Exam;

	A$\beta-$ (n = 26)	**A$\beta+$ (n = 21)**	***t* or $\chi 2$**	***p*-value**
Age (years)	78.7 (7.0)	78.1 (3.6)	0.38	0.71
Sex (female)	17 (65%)	14 (67%)	0.01	0.93
Education (years)	17.0 (1.9)	16.0 (2.1)	1.66	0.10
ApoE4 (+)	2 (8%)	15 (75%)[a]	21.98	< 0.001
MMSE	29.1 (1.0)	28.3 (1.4)	2.15	0.04
Global PiB DVR	1.01 (0.02)	1.37 (024)	−6.86	< 0.001
Time difference (days)	99 (124)	73 (79)	0.87	0.39

[a]One A$\beta+$ subject missing APOE data.

Table II

Selection performance over 100 data replications in the simulation study. We compare three methods, the voxel-wise analysis, the region-wise analysis, and our proposed spatially adaptive analysis. We also examine the effect of pre-smoothing and the percentile thresholding value.

Pre-smoothing	Signal	Method	Type	Sensitivity	Specificity	FDR
No	Weak	Voxel-wise	Positive	0.000 (0.001)	1.000 (0.000)	0.269 (0.439)
			Negative	0.001 (0.003)	1.000 (0.000)	0.059 (0.243)
		Region-wise	Positive	0.221 (0.207)	0.957 (0.040)	0.746 (0.035)
			Negative	0.474 (0.006)	0.957 (0.011)	0.626 (0.031)
		Spatially adaptive (0.90)	Positive	0.836 (0.099)	0.971 (0.006)	0.344 (0.058)
			Negative	0.973 (0.032)	0.968 (0.007)	0.383 (0.048)
		Spatially adaptive (0.95)	Positive	0.624 (0.096)	0.994 (0.002)	0.137 (0.061)
			Negative	0.854 (0.053)	0.994 (0.002)	0.125 (0.037)
	Medium	Voxel-wise	Positive	0.009 (0.012)	1.000 (0.000)	0.021 (0.133)
			Negative	0.016 (0.022)	1.000 (0.000)	0.030 (0.165)
		Region-wise	Positive	0.627 (0.194)	0.876 (0.045)	0.745 (0.021)
			Negative	0.475 (0.009)	0.957 (0.013)	0.628 (0.034)
		Spatially adaptive (0.90)	Positive	0.986 (0.015)	0.962 (0.003)	0.365 (0.018)
			Negative	0.999 (0.003)	0.958 (0.005)	0.442 (0.029)
		Spatially adaptive (0.95)	Positive	0.749 (0.047)	0.997 (0.002)	0.060 (0.038)
			Negative	0.909 (0.028)	0.995 (0.001)	0.090 (0.028)
	Strong	Voxel-wise	Positive	0.048 (0.038)	1.000 (0.000)	0.000 (0.000)
			Negative	0.098 (0.094)	1.000 (0.000)	0.003 (0.025)
		Region-wise	Positive	0.743 (0.110)	0.849 (0.031)	0.751 (0.027)
			Negative	0.477 (0.013)	0.953 (0.019)	0.638 (0.052)
		Spatially adaptive (0.90)	Positive	0.995 (0.006)	0.960 (0.001)	0.378 (0.006)
			Negative	1.000 (0.001)	0.953 (0.004)	0.469 (0.020)
		Spatially adaptive (0.95)	Positive	0.768 (0.040)	0.998 (0.002)	0.040 (0.033)
			Negative	0.922 (0.029)	0.996 (0.002)	0.078 (0.029)
Yes	Weak	Voxel-wise	Positive	0.003 (0.004)	1.000 (0.000)	0.026 (0.145)
			Negative	0.026 (0.040)	1.000 (0.000)	0.019 (0.117)
		Region-wise	Positive	0.221 (0.210)	0.957 (0.040)	0.748 (0.045)

Pre-smoothing	Signal	Method	Type	Sensitivity	Specificity	FDR
			Negative	0.474 (0.006)	0.957 (0.013)	0.628 (0.036)
		Spatially adaptive (0.90)	Positive	0.961 (0.033)	0.966 (0.004)	0.350 (0.031)
			Negative	0.998 (0.006)	0.960 (0.005)	0.433 (0.033)
		Spatially adaptive (0.95)	Positive	0.731 (0.053)	0.996 (0.002)	0.078 (0.040)
			Negative	0.910 (0.027)	0.995 (0.001)	0.090 (0.026)
	Medium	Voxel-wise	Positive	0.157 (0.111)	1.000 (0.000)	0.000 (0.000)
			Negative	0.260 (0.169)	1.000 (0.000)	0.001 (0.005)
		Region-wise	Positive	0.617 (0.210)	0.878 (0.048)	0.745 (0.021)
			Negative	0.476 (0.010)	0.955 (0.015)	0.631 (0.041)
		Spatially adaptive (0.90)	Positive	0.997 (0.004)	0.960 (0.001)	0.378 (0.004)
			Negative	1.000 (0.000)	0.952 (0.003)	0.479 (0.014)
		Spatially adaptive (0.95)	Positive	0.780 (0.024)	0.998 (0.001)	0.029 (0.023)
			Negative	0.934 (0.023)	0.997 (0.001)	0.066 (0.023)
	Strong	Voxel-wise	Positive	0.455 (0.129)	1.000 (0.000)	0.000 (0.000)
			Negative	0.582 (0.226)	1.000 (0.000)	0.000 (0.003)
		Region-wise	Positive	0.746 (0.108)	0.844 (0.036)	0.756 (0.032)
			Negative	0.478 (0.014)	0.950 (0.022)	0.646 (0.061)
		Spatially adaptive (0.90)	Positive	0.999 (0.002)	0.960 (0.000)	0.379 (0.001)
			Negative	1.000 (0.000)	0.950 (0.002)	0.489 (0.011)
		Spatially adaptive (0.95)	Positive	0.788 (0.023)	0.999 (0.001)	0.019 (0.020)
			Negative	0.943 (0.020)	0.997 (0.001)	0.057 (0.020)

Table III

Selection performance over 100 data replications with different values of $\tilde{d}$ in graph-based partition.

$\tilde{d}$	Type	Sensitivity	Specificity	FDR
1	Positive	0.690 (0.087)	0.998 (0.001)	0.037 (0.021)
	Negative	0.906 (0.049)	0.998 (0.001)	0.044 (0.019)
2	Positive	0.745 (0.047)	0.997 (0.001)	0.055 (0.030)
	Negative	0.919 (0.027)	0.996 (0.001)	0.076 (0.021)
3	Positive	0.731 (0.051)	0.996 (0.002)	0.077 (0.039)
	Negative	0.907 (0.027)	0.995 (0.001)	0.092 (0.027)
4	Positive	0.738 (0.044)	0.996 (0.002)	0.076 (0.040)
	Negative	0.905 (0.032)	0.995 (0.002)	0.094 (0.032)
5	Positive	0.694 (0.069)	0.994 (0.003)	0.121 (0.064)
	Negative	0.878 (0.051)	0.994 (0.003)	0.122 (0.051)
7	Positive	0.618 (0.079)	0.989 (0.005)	0.211 (0.089)
	Negative	0.824 (0.090)	0.991 (0.004)	0.173 (0.084)
9	Positive	0.546 (0.094)	0.984 (0.005)	0.302 (0.108)
	Negative	0.711 (0.064)	0.985 (0.003)	0.289 (0.063)
10	Positive	0.493 (0.082)	0.981 (0.005)	0.363 (0.095)
	Negative	0.670 (0.053)	0.983 (0.003)	0.330 (0.053)
11	Positive	0.461 (0.086)	0.979 (0.005)	0.410 (0.100)
	Negative	0.634 (0.038)	0.981 (0.002)	0.366 (0.038)

Table IV

Negative correlations between AV-1451 and FDG, for Aβ-NEGATIVE AND Aβ-positive participants, following VBM correction. The mean voxel correlation is the average of voxel-wise correlations for all the voxels in the spatially adaptively identified regions. The region correlation is the correlation estimated by our spatially adaptive method, i.e., the estimated r_g in (3). The p-value is obtained based on the likelihood ratio test on the correlation between the two modalities. We only report those clusters that our test, after multiple testing correction, found significant correlation p-value smaller than 0.05, and with no fewer than 20 voxels per cluster. The AAL atlas was used to describe spatial locations of our findings but not used in our detection method.

Aβ− participants:					
AAL region	cluster center	cluster size	mean voxel correlation	region correlation	p-value
ParaHippocampal_R	(2.6, −5.9, −413)	286	−0.347	−0.12	$< 1e-8$
Occipital_Inf_L	(−40.4, −88.5, −25.7)	123	−0.306	−0.10	$< 1e-8$
Hippocampus_L	(−46.9, −17.5, −32.2)	113	−0.374	−0.13	$< 1e-8$
Frontal_Mid_Orb_R	(7.3, 41.5, −28.9)	21	−0.353	−0.12	$< 1e-8$
Lingual_R	(−9.3, −78.3, −20.3)	35	−0.364	−0.12	$< 1e-8$
Occipital_Mid_L	(−62.0, −85.2, −15.5)	26	−0.314	−0.10	$1.20e-5$
Ihsula_R	(13.4, 30.4, −13.2)	35	−0.341	−0.11	$< 1e-8$
Aβ+ participants:					
AAL region	cluster center	cluster size	mean voxel correlation	region correlation	p-value
Fusiform_R	(10.3, 1.5, −54.1)	19	−0.472	−0.16	$< 1e-8$
Temporal_Pole_Mid_L	(−56.2, 103, −52.5)	12	−0.439	−0.15	$6.60e-7$
Temporal_Inf_R	(25.8, −35.4, −37.1)	49	−0.429	−0.14	$< 1e-8$
Rectus_R	(−12.2, 26.1, −32.6)	122	−0.407	−0.14	$< 1e-8$
Rectus_L	(−32.5, 21.7, −33.5)	37	−0.429	−0.14	$< 1e-8$
Frontal_Mid_Orb_L	(−45.2, 38.7, −30.4)	75	−0.393	−0.13	$< 1e-8$
Cingulum_Post_L	(−24.4, −45.7, 7.3)	139	−0.352	−0.12	$< 1e-8$
Cingulum_Mid_L	(−30.3, 4.3, 21.7)	23	−0.468	−0.16	$2.10e-8$
Frontal_Mid_L	(−42.6, 23.2, 22.8)	25	−0.360	−0.12	$9.30e-8$
Front al_Mid_L	(−55.8, 13.1, 36.2)	110	−0.352	−0.12	$< 1e-8$